Letters

Analysis and Optimization of Current Coupling Control in Flux-Weakening Region of PMSM

Xu Zhang, *Member, IEEE*, Zhe Chen, and Yongchang Zhang, *Senior Member, IEEE*

***Abstract*—Different from the independent control of *dq*-axis current ($i_{sd,q}$) in the base-speed region, the flux-weakening (FW) region requires coupling control of $i_{sd,q}$ to satisfy the maximum voltage constraint. This article revealed the reasons for the failure of the rapid current coupling control in FW region from the perspectives of control structure and vector trajectory. The direct and indirect coupling model (DCM and ICM) are quantitatively calculated and compared. The ICM is proved to have higher accuracy than DCM, which is used to optimize the current following performance and suppress voltage fluctuation during transition process between maximum and nonmaximum torque condition. Finally, the comparative experiments verified the analysis-correctness and superiority of the proposed method.**

***Index Terms*—Coupling model, dynamic improvement, flux-weakening (FW) control, permanent magnet synchronous motor.**

I. Introduction

IN FLUX-WEAKENING (FW) region, the increase of stator voltage can improve the maximum output torque, or reduce the amplitude of stator current for efficiency improvement in nonmaximum torque condition. But when the voltage exceeds the maximum value, the voltage saturation and degeneration of dynamic performance can be caused. Thus, the maximum voltage output is the core objective of FW control, for performance optimization and avoiding voltage saturation.

To achieve the maximum voltage control, the flux current component needs to adaptively change with torque and frequency, meaning that the coupling control between *dq*-axis current is demanded in FW region. In [1] and [2], the current coupling control is realized according to voltage control [1] and motor model [2], respectively. But the coupling control can only realize in maximum torque condition through the current limitation structure. Focusing on this problem, the conventional algorithms can be divided into four categories for the current coupling control in FW region: adaptive parameters [3], [4], priority control of i_{sd} [5], [6], vector trajectories optimization [7], [8], and controller structure optimization [9], [10]. Table I shows the characteristics of the conventional methods.

In [3] and [4], the parameters of FW controller are designed to adaptively change with rotor speed to optimize the dynamic performance in high speed condition. However, the design process of parameters is complex. Besides, the parameters are not designed directly adaptive to the error of voltage amplitude. Thus, the voltage fluctuations in dynamic process is remained to be suppressed, especially during transition process between nonmaximum torque and maximum torque conditions. In [5] and [6], the priority control of i_{sd} is realized by the limitation of u_{sq} and coupling compensation of $u_{sd,q}$, respectively. However, the priority control of i_{sd} is realized based on the exceeding part of voltage vector. Thus, this kind of methods utilizes the voltage overshoot rather than suppressing it, leading to the limited suppression effect on voltage saturation. In [7] and [8], the trajectories of voltage and current vector are optimized. But the method is designed for specific working conditions: transition from based speed region to FW region [7] and transition from maximum torque to nonmaximum torque [8]. In [9], the two current controller structure are replaced with single current controller. The voltage saturation can be eliminated. Nevertheless, the stable operating range of the method is limited. And the handoff is needed between base-speed region and FW region. In [10], the PI-type FW controllers are changed to combination of low-pass filter and high-pass filter. Although the dynamic performance is improved, the steady-state noise can be introduce to the system. Therefore, conventional methods cannot satisfy the requirements of current coupling control in diverse dynamic processes. In nonmaximum torque condition, especially the transition process between maximum and nonmaximum torque, how to achieve rapid coupling control between *dq*-axis current still needs to be studied.

Focusing on the above problems, the contribution of this letter is to summarize the reasons for the failure of current coupling control in FW region. On this basis, the indirect coupling model (ICM) is quantitatively calculated and applied for rapid current coupling control.

Manuscript received 3 May 2024; revised 3 June 2024; accepted 21 June 2024. Date of publication 26 June 2024; date of current version 4 September 2024. This work was supported in part by Beijing Natural Science Foundation under Grant 3244050, in part by the China National Postdoctoral Program for Innovative Talents under Grant BX20230119, in part by the National Key R&D Program of China under Grant 2023YFB4203400, in part by China Postdoctoral Science Foundation funded project under Grant 2023M741149, and in part by the Fundamental Research Funds for the Central Universities under Grant 2024MS008. *(Corresponding author: Yongchang Zhang.)*

The authors are with the School of Electrical and Electronic Engineering, North China Electric Power University, Beijing 102206, China (e-mail: zhangxu@ncepu.edu.cn; 120232201665@ncepu.edu.cn; yozhang@ieee.org).

Color versions of one or more figures in this article are available at https://doi.org/10.1109/TPEL.2024.3419146.

Digital Object Identifier 10.1109/TPEL.2024.3419146

TABLE I
COMPARISON OF DIFFERENT FW METHODS

	Methods	Structure optimization of FW loop	Number of PI controller in FW loop	Sensitivity to parameter changes	Voltage fluctuations during changes of i_{sq} and ω_e	Remarks
1	Adaptive parameters of FW controller [3]	No	3	High	Medium	Failure to consider voltage fluctuations from i_{sq} changes
2	Unified design of controller parameters [4]	Yes	3	High	Medium	
3	Limitation of u_{sd} [5]	No	3	Low	High	Utilizes the voltage overshoot rather than suppressing it
4	Voltage Reference Modification [6]	Yes	3	Low	High	
5	Smooth transition to FW condition [7]	No	3	Low	Medium	Designed for specific condition
6	Rapid convergence to steady state point [8]	No	3	High	High	
7	Single current control [9]	Yes	2	High	Low	Handoff is needed
8	Proposed method	Yes	1	Medium	Low	/

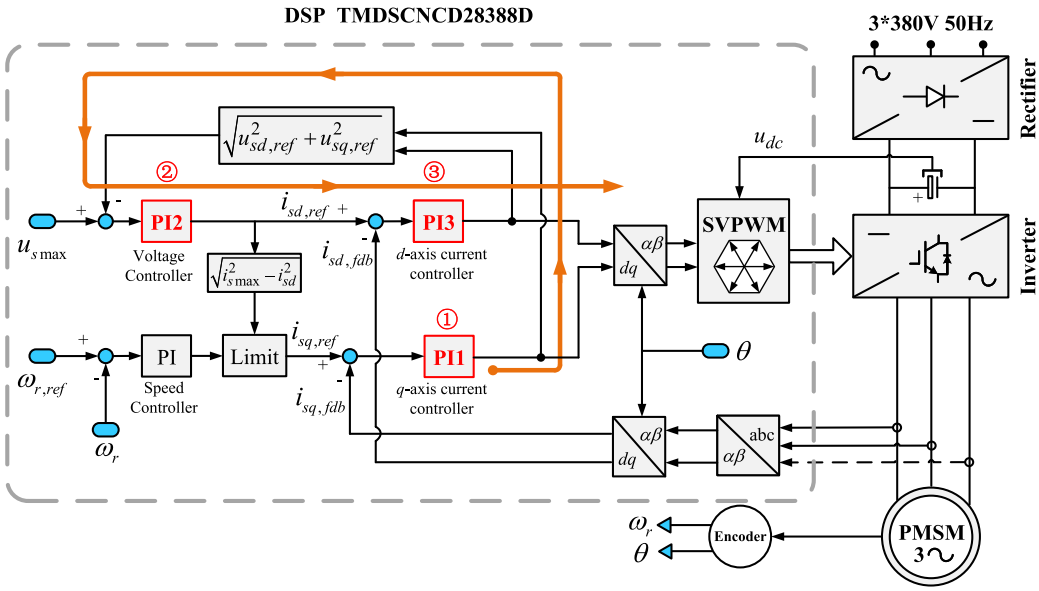

Fig. 1. Block diagram of the voltage closed-loop based FW system.

II. PROBLEM ANALYSIS OF CURRENT COUPLING CONTROL IN FW REGION OF PMSM

A. Basic Theory

In the rotor flux-oriented control (RFOC)-based PMSM driving system, the stator voltage equation in the synchronous rotating frame can be expressed as

$$\begin{cases} u_{sd} = R_s i_{sd} + L_d p i_{sd} - \omega_e L_q i_{sq} \\ u_{sq} = R_s i_{sq} + L_q p i_{sq} + \omega_e (L_d i_{sd} + \psi_F) \end{cases} \tag{1}$$

where $u_{sd,q}$ are the d,q-axis stator voltages; $i_{sd,q}$ are the d,q-axis stator currents; ψ_F is the permanent magnet flux linkage; R_s is the stator resistance; $L_{d,q}$ are the d,q-axis stator inductance; ω_e is the synchronous frequency; and p is the differential operator.

According to (1), the stator voltage amplitude is directly proportional to synchronous frequency. When the amplitude of stator voltage exceeds the voltage constraint along with the increasing speed, the FW operation is needed to pull back the exceeding voltage. Thus, as shown in Fig. 1, the voltage controller is employed for maximum voltage control.

In Fig. 1, the control architecture diagram includes three-phase power supply, rectifier, inverter, control scheme, motor, etc. The control algorithm is embedded within the DSP, which executes the necessary control functions for the system. The structure diagram of the voltage closed-loop based FW scheme is shown in the gray dashed box in Fig. 1. The switching signal of the inverter is calculated through the SVPWM module, so as to control the turn-ON and turn-OFF of the inverter. The dc-Link voltage is obtained from the grid voltage by the uncontrollable rectification.

Under the adjustment of voltage controller, the voltage amplitude satisfies (2) in FW region

$$u_{sd}^2 + u_{sq}^2 = u_{s\max}^2. \tag{2}$$

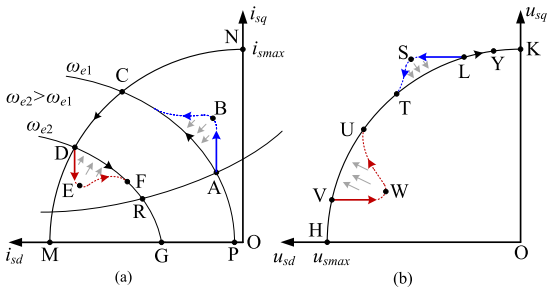

Fig. 2. (a) Current vector trajectory. (b) Voltage vector trajectory.

According to (1), the ratio of the resistive voltage term decreases with the increase of ω_e. In high-speed condition, the stator voltage terms play a very small part in (1). To facilitate the calculation of the parametric equation of current vector trajectory, the stator voltage terms and the transient terms in (1) can be neglected and rewritten as [6]

$$u_{sd} = -\omega_e L_q i_{sq}, u_{sq} = \omega_e (L_d i_{sd} + \psi_F). \tag{3}$$

By substituting (3) into (2), the parametric equation of current vector trajectory can be obtained as

$$(\omega_e L_q)^2 i_{sq}^2 + \omega_e^2 \left(L_d i_{sd} + \psi_F\right)^2 = u_{s\max}^2. \tag{4}$$

The current limitation can be expressed as

$$i_{sd}^2 + i_{sq}^2 \le i_{smax}^2. \tag{5}$$

According to (2), (4), and (5), Fig. 2 shows the trajectories of voltage and current vectors in FW region. Based on Figs. 1 and 2, the current coupling problem of FW control of PMSM is analyzed in Section II-B.

B. Problem Analysis of Current Coupling Control

As shown in Fig. 2(a), the current trajectory can be divided into three segments: transition from nonmaximum to maximum torque (AC segment), maximum torque output (CD segment), and the transition from maximum to nonmaximum torque (DF segment). In the maximum torque output condition during the step-acceleration process, since i_{sq} is equal to the maximum value i_{sqmax} (determined by i_{sd}), the voltage controller can adjust i_{sd} and i_{sq} simultaneously by controlling i_{sd}. Thus, the voltage controller has the coupling control ability between dq-axis current. On this basis, the current vector can move along the maximum torque trajectory.

However, during the transition processes between maximum and nonmaximum torque condition, i_{sq} is below i_{sqmax} and is determined by the speed controller. Since the voltage controller fails to simultaneously control i_{sd} and i_{sq}, the voltage controller loses the ability of current coupling control. When the system enters dynamic states due to the changes of load torque or speed reference, i_{sqref} changes before i_{sdref}. And then, the changes of i_{sqref} lead to the increase (acceleration or load increase) or decrease (deceleration or load decrease) of voltage amplitude. Then, i_{sd} is need to be adjusted to suppress the voltage ripples. However, due to the inability to directly adjust i_{sdref} according to the changes in i_{sqref}, the control of i_{sd} relies on voltage controller. But the voltage controller cannot predict the voltage utilization of voltage), and can only operate after the voltage ripples appear, leading to control delay of i_{sd}. Meanwhile, as shown in Fig. 1, there are three PI-type controllers to realize the coupling control between i_{sd} and i_{sq}. They are: q-axis current controller (causing voltage changes), voltage controller (adjusting i_{sdref}), and d-axis current controller (realizing change of i_{sd}). Due to the triple connected controller, the current coupling control cannot realize immediately, leading to degradation of dynamic performance.

Coupling Control Problem Reflected in Trajectories: Fig. 2 shows the trajectories of current and voltage vectors during the acceleration process from ω_{e1} to ω_{e2}. In Fig. 2(a), the curve PC and GD are the voltage constraint at ω_{e1} and ω_{e2} ($\omega_{e2}>\omega_{e1}$) [the parametric equation in (4)], respectively. MN is current limiting boundary. Point A is the initial point. When speed reference increase, the working point is expected to move to C to output the maximum torque for speed following. The ideal trajectory is AC. However, due to the failure of current coupling control, the i_{sd} cannot immediately decrease along with the increasing i_{sq}, and then, the actual trajectory (ABC) deviates from ideal trajectory. Correspondingly, as shown in Fig. 2(b), the voltage trajectory (LST) exceeds the voltage limiting boundary (HK). When the speed reach the reference value ω_{e2}, the maximum torque is not demanded, i_{sq} decreases. Similarly, i_{sd} cannot immediately increase along with the decreasing i_{sq}. The actual current trajectory (DEF) deviates from ideal trajectory (DF). Correspondingly, the voltage trajectory (VWU) drops from the voltage limiting boundary (HK). Therefore, the slow coupling control causes voltage and current fluctuations. Finally, when the current returns to the DF and moves from point F to point R along the voltage constraint ellipse in Fig. 2(a), the voltage vector in Fig. 2(b) moves along the voltage limitation circle from point U to point Y and enters to the new steady state.

In conclusion, the failure of current coupling control can be attributed to two aspects. 1) Due to the lack of direct control pathway from q-axis to d-axis current, the d-axis current cannot perceive or adaptively adjust with the change of q-axis current. 2) The cascade structure of triple PI-type controllers causes control delay, making it impossible to achieve rapid current coupling control.

III. Propose Current Coupling Control Method In FW Region

To realize rapid coupling control between dq-axis currents in FW region, this article analyses the error of current coupling model, and then, designs the coupling pathway from q-axis to d-axis current.

A. Quantitative Analysis of Current Coupling Model in FW Region

According to (4), i_{sd} can be expressed as the function of i_{sq} and ω_e

$$\begin{aligned} i_{sd} &= g\left(\omega_e, i_{sq}\right) \\ &= \left(\sqrt{\frac{u_{s\,max}^2 - (\omega_e L_q i_{sq})^2}{2}} - \psi_F\right) / L_d. \end{aligned} \tag{6}$$

Equation (6) can be regarded as the direct coupling model (DCM) between i_{sd} and i_{sq}. When i_{sq} and ω_e changes, the current coupling can be realized by control i_{sd} change with reference to (6). However, in FW region, L_d and L_q is affected by the changes of both i_{sd} and i_{sq} (especially the interior-type PMSM). The accuracy of DCM is affected by L_d and L_q. Considering the changes of L_d and L_q, (6) can be rewritten as

$$\begin{aligned} i_{sd} &= f(\omega_e, i_{sq}, \Delta L_d, \Delta L_q) \\ &= \frac{\left\{\sqrt{\frac{u_{s\,max}^2 - [\omega_e(L_q+\Delta L_q)i_{sq}]^2}{\omega_e^2}} - \psi_F\right\}}{(L_d + \Delta L_d)} \\ &= g(\omega_e, i_{sq}) + h(\omega_e, i_{sq}, L_d, L_q, \Delta L_d, \Delta L_q) \end{aligned} \tag{7}$$

where $h(\omega_e, i_{sq}, L_d, L_q, \Delta L_d, \Delta L_q)$ represents error of the DCM.

The $h(\omega_e, i_{sq}, L_d, L_q, \Delta L_d, \Delta L_q)$ can be obtained by subtracting (6) from (7). Since the variation range of i_{sq} decreases in high-speed condition, the ΔL_q that can be caused by the changes of i_{sq} is also reduced. Thus, the ΔL_q is set to zero for ease of obtaining the explicit expression of $h(\omega_e, i_{sq}, L_d, L_q, \Delta L_d, \Delta L_q)$

$$\begin{aligned} &h(\omega_e, i_{sq}, L_d, L_q, \Delta L_d, \Delta L_q) \\ &= \left[\frac{\sqrt{u_{s\,max}^2 - (\omega_e L_q i_{sq})^2}}{\omega_e} - \psi_F\right] \frac{\Delta L_d}{(L_d + \Delta L_d)L_d}. \end{aligned} \tag{8}$$

Actually, since the steady-state value can be determined by the voltage control loop, the absolute value of i_{sd} is not required. Only the relative change value of i_{sd} is required during speed or load changes, which cannot provided by the voltage controller in time. The relative i_{sd} change can be applied as the indirect coupling component, which can be expressed as

$$\begin{aligned} \Delta i_{sd} &= i_{sd1} - i_{sd0} \\ &= f(\omega_{e0} + \Delta\omega_e, i_{sq0} + \Delta i_{sq}, \Delta L_d, \Delta L_q) \\ &\quad - f(\omega_{e0}, i_{sq0}, \Delta L_d, \Delta L_q) \\ &= [g(\omega_{e0} + \Delta\omega_e, i_{sq0} + \Delta i_{sq}) - g(\omega_{e0}, i_{sq0})] \ldots Aterm \\ &\quad + [h(\omega_{e0} + \Delta\omega_e, i_{sq0} + \Delta i_{sq}, L_d, L_q, \Delta L_d, \Delta L_q) \\ &\quad - h(\omega_{e0}, i_{sq0}, L_d, L_q, \Delta L_d, \Delta L_q)] \ldots\ldots\ldots\ldots\ldots Bterm \end{aligned} \tag{9}$$

where i_{sd0}, i_{sq0}, and ω_{e0} are the initial values of *dq*-axis current and operation frequency, respectively; $\Delta\omega_e$ and Δi_{sq} are the changes value of ω_e and i_{sq} during the dynamic process, respectively; *B* term represents error of the ICM.

According to the *B* term in (9), the error of the ICM is equal to the variation value of the DCM error during the dynamic process. According to (8), the positive or negative of the error of direct decoupling model is not affected by $\Delta\omega_e$ and Δi_{sq}. Thus, the $h(\omega_e + \Delta\omega_e, i_{sq} + \Delta i_{sq}, L_d, L_q, \Delta L_d, \Delta L_q)$ and $h(\omega_e, i_{sq}, L_d, L_q, \Delta L_d, \Delta L_q)$ in the *B* term in (9) are both positive or negative. Therefore, the error of the indirect decoupling model is smaller than that of the direct decoupling model.

According to (6), (7), and (9), Fig. 3 shows the quantitative calculation results of errors of the DCM and ICM. The used motor parameters are as follows: $R_s = 1.426\Omega$; $L_d = L_q = 0.0188$ H, $\psi_F = 0.318$ Wb, the number of pole pairs is 5. Fig. 3 shows the errors of DCM and ICM under variations of L_q and L_d. In Fig. 3, the changes in inductance are divided into two condition: $\Delta L_q = \pm 0.5 L_q$, $\Delta L_d = 0$ and $\Delta L_q = 0$, $\Delta L_d = \pm 0.5 L_d$. The errors of DCM are obtained by subtracting (6) from (7). While the errors of ICM are obtained by substituting the certain values of $\Delta i_{sq}, \Delta\omega_e, \omega_e, i_{sq}$, and $\Delta L_{d,q}$ to the *B* term in (9). The substituted Δi_{sq} and $\Delta\omega_e$ are set to two categories: $\Delta i_{sq} = 0.3 i_{smax}$, $\Delta\omega_e = 0$ and $\Delta i_{sq} = 0$, $\Delta\omega_e = 0.3\omega_{e\text{-rated}}$. According to Fig. 3, the errors of ICM are smaller than those of DCM when $L_{d,q}$ changes. Thus, this article applies the ICM for current coupling control in FW region.

B. Propose Current Coupling Control Method

Based on the ICM derived in Section III-A, the coupling component of i_{sd} can be obtained by substituting $\Delta\omega_e$ and Δi_{sq} to (9). When the coupling component is applied to *d*-axis current, the reference current value need to satisfy the current limitation

$$(i_{sd0} + \Delta i_{sd})^2 + i_{sq0}^2 \le i_{s\,max}^2 \tag{10}$$

where i_{sd0} and i_{sq0} are the initial values of *dq*-axis current, respectively, Δi_{sd} is the coupling component.

By substituting (6) into (10), the limitation of the coupling component Δi_{sd} can be expressed as (11) (shown at the bottom of the next page). Fig. 4 shows the block diagram of the proposed current coupling control method. The coupling control module is divided into two sub modules: dynamic state judgement (DSJ) module and ICM module. When the following errors of i_{sq} or ω_e appear, the system enters the dynamic process, and then, the DSJ module output the trigger signal. The trigger signal is inputted to the latches of i_{sq} and ω_e, and then, the initial values of can be saved as i_{sq0} and ω_{e0}. On this basis, the Δi_{sq} and $\Delta\omega_e$ can be obtained as i_{sq}-i_{sq0} and ω_e-ω_{e0}, respectively. By substituting Δi_{sq} and $\Delta\omega_e$ into the ICM module, the decoupling component of i_{sd} can be obtained as $i_{sd\text{-}A}$. On the other hand, when the system returns to the steady state, the trigger signal control the latches no longer work, and then, ω_{e0} and i_{sq0} are equal to i_{sq} and ω_e, respectively. $i_{sd\text{-}A}$ is controlled to zero with $\Delta i_{sq} = 0$ and $\Delta\omega_e = 0$. To avoid the abrupt change of the decoupling current, the $i_{sd\text{-}A}$ is accumulated to $i_{sd\text{-}B}$ when the system returns to steady state. The sum of $i_{sd\text{-}A}$ and $i_{sd\text{-}B}$ is used as the final coupling component $i_{sd\text{-}cp}$. $i_{sd\text{-}cp}$ is added to i_{sdref}. On this basis, as shown in Fig. 2, the current vector trajectory can be corrected from ABC to AC when i_{sq} increases, and from DEF to DF when i_{sq} decreases.

Fig. 5 shows the bode diagram of the proposed method and conventional method. The calculation of the closed loop functions of the proposed method and conventional method is given in Appendix. Besides, it is proved in Appendix that the proposed method does not affect the system stability. According to Fig. 5, the amplitude frequency characteristic curve of the proposed method is higher than that of the conventional method, meaning

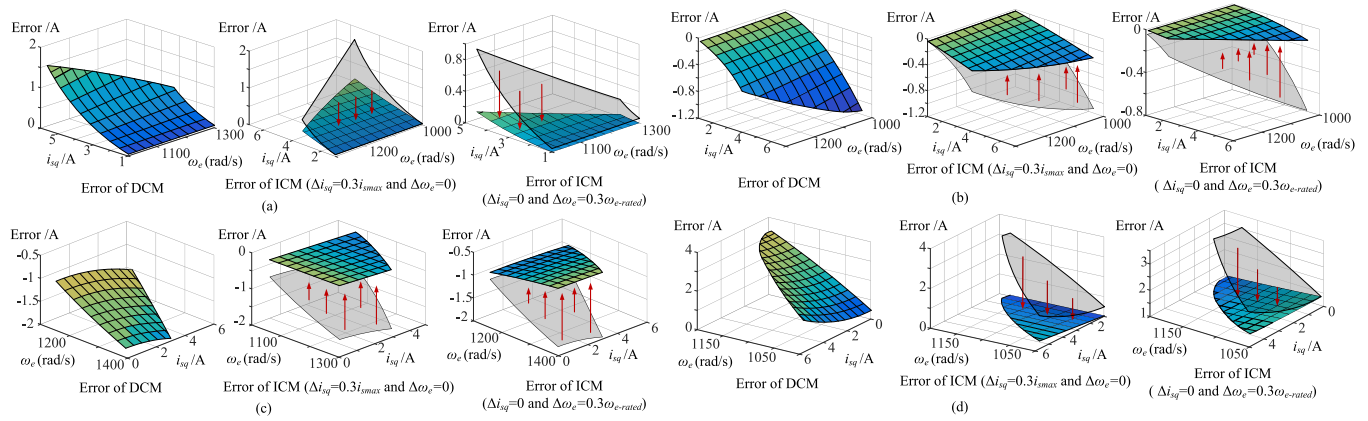

Fig. 3. Quantitative calculation results of errors of DCM and ICM. (a) $\Delta L_q = +0.5L_q$, $\Delta L_d = 0$. (b) $\Delta L_q = -0.5L_q$, $\Delta L_d = 0$. (c) $\Delta L_q = 0$, $\Delta L_d = +0.5L_d$. (d) $\Delta L_q = 0$, $\Delta L_d = -0.5L_d$.

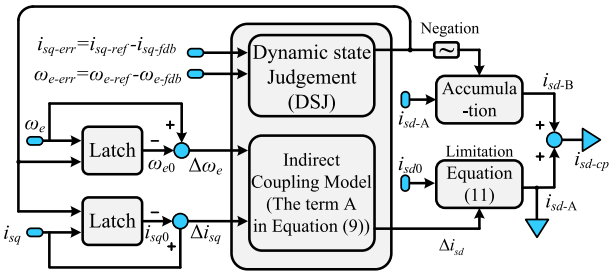

Fig. 4. Block diagram of the optimized current coupling control method.

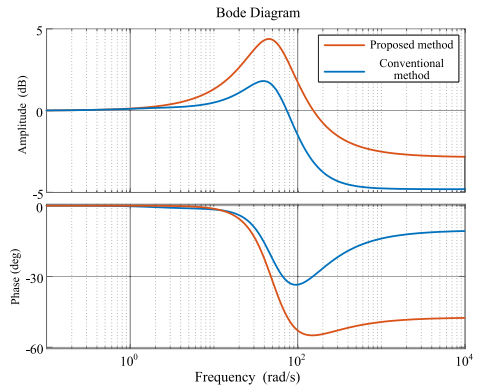

Fig. 5. Bode diagram of closed loop transfer function of the proposed method and conventional method.

that the proposed method can improve the system dynamic performance.

C. Discussion of the method complexity

According to Fig. 4, the proposed method does not contain the PI controller. Thus, when the motor is changed in actual application, there is no need to re-tune the controller parameters, which is convenient for the practical application of the algorithm.

Then, the computational burden increased from the proposed method is very little. The computational load of the proposed indirect decoupling control and the conventional control method is compared on the rapid control prototype platform based on TMDSCNCD28388D. The number of clock cycles for the two methods is shown in Table II.

TABLE II
CLOCK CYCLE NUMBER

Control method	Clock cycle number
Conventional decoupled control	12106
Proposed non-direct current control	12553

The clock frequency of the DSP control board is 200 MHz, and the program calculation time is 60.53 μs with the traditional method and 62.76 μs with the proposed method. Although the computational load of the proposed method is higher than that of the traditional method, the increase is relatively small, about 3.6%.

Further, the structure of the proposed method has the potential to be further simplified in actual application, which can reduce the method complexity.

In Fig. 4, the changing values ($i_{sd\text{-}A}$) is independent from the compensation to i_{sd} (i.e., the $i_{sd,cp}$ in Fig. 4) for the ease of test of the ICM model. In actual application, there is another design idea that can achieve a similar compensation effect. That is directly input the ω_e and i_{sq} to the motor model. The initial values (i_{sq0} and ω_{e0}) and changing (Δi_{sq} and $\Delta\omega_e$) values of ω_e and i_{sq} are no longer treated separately. Correspondingly, the initial ($i_{sd\text{-}B}$) and changing values ($i_{sd\text{-}A}$) of the compensation to i_{sd} merge into one variable. To avoid the overcompensation, an

$$\Delta i_{sd} \le \frac{-2\omega_e^2 L_d\psi_F + \sqrt{\left(2\omega_e^2 L_d\psi_F\right)^2 - 4\left[\omega_e^2\left(L_d^2 - L_q^2\right)\right]\cdot\left[\left(\omega_e L_q i_{smax}\right)^2 + \left(\omega_e\psi_F\right)^2 - u_{smax}^2\right]}}{2\left[\omega_e^2\left(L_d^2 - L_q^2\right)\right]} - i_{sd0} \tag{11}$$

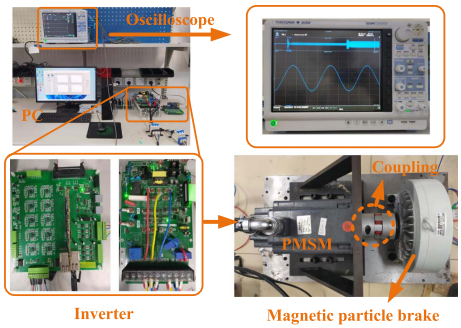

Fig. 6. Photograph of the experimental platform.

TABLE III
MEAN ABSOLUTE ERROR CALCULATION RESULTS

Working conditions	Variables	Without proposed method	With proposed method
Step acceleration	i_{sd}	1.60 A	1.15 A
	i_{sq}	2.27 A	1.51 A
	u_{fdb}	0.43 V	0.21 V
sudden application of 30% rated load	i_{sd}	0.52 A	0.29 A
	i_{sq}	0.53 A	0.32 A
	u_{fdb}	0.13 V	0.06 V

overall limiting to the combined compensation value is required. In this way, the latching structure of the input of ICM in Fig. 4 can be omitted, thereby simplifying the structure.

IV. EXPERIMENTAL RESULTS

The proposed current coupling optimization method was validated on a rapid control prototyping platform based on TMDSC-NCD28388D. Fig. 6 shows the photograph of the experimental platform. The LabVIEW-based host-PC interface of the platform enables the observation and recording of all internal variable values in each control cycle. The maximum current is 10 A. For safety concern, the maximum voltage of system is set to 155 V to limit the maximum speed of the PMSM. On this basis, the base speed is 750 r/min. The SVPWM switching frequency is 10 kHz. The bandwidth of current loop is set to 800 Hz.

Fig. 7 shows the comparison of the system responses during step acceleration from 90 Hz (1080 r/min) to 140 Hz (1680 r/min) with and without the proposed method. As shown in Fig. 7(a), the step acceleration leads to step increases in both $i_{sq\text{-}ref}$ and u_{fdb} (feedback value of voltage controller). It can be seen that the obvious voltage overshoot exists before u_{ref} restored to u_{smax} (p.u. $= 1$). When u_{fdb} exceeds u_{smax}, it can be seen that the voltage saturation leads to the decrease in the following ability of i_{sd} and i_{sq}. Due to the failure of $i_{sd\text{-}fdb}$ to quickly follow its reference value, the voltage overshoot rises first [from A to B in u_{fdb} waveform in Fig. 7(a)], and then gradually decreases. It takes about 30ms for u_{fdb} to restored to u_{smax}. As for the optimized method in Fig. 7(b), it can be seen that the following performance of i_{sd} is improved with the d-axis current priority control. However, since the d-axis current priority control is realized by increasing the distribution of d-axis voltage and decreasing the q-axis voltage, the following performance of i_{sq} is not good. Besides, since the d-axis current priority control relies on the optimized distribution of the exceeding voltage, the effect on suppression of voltage overshoot is limited. And due to the relies on the exceeding voltage, when the voltage fluctuates downward due to the decreasing i_{sq}, the method is not effective for suppressing the downward voltage fluctuations. According to the enlarged view of voltage drop in Fig. 7(b), it can be seen that the voltage fluctuation is same with the conventional method, which also takes 86 ms for u_{fdb} to restored to u_{smax}. The method in [6] optimizes dynamic performance from the improvement of voltage distribution, which is not contradict but compatible with the method in this article.

By contrast in Fig. 7(c), the more precise adjustment to i_{sd} is realized with the proposed method during dynamic process. It can be seen that the overshoot of u_{fdb} decreases rapidly. It takes about 18 ms for u_{fdb} to restored to u_{smax}. The time required for voltage desaturation is reduced by 40% compared to the conventional method in Fig. 7(a). The following performances of the i_{sd} and i_{sq} are both improved. Moreover, when i_{sq} decreases after the speed reaches the reference value, the voltage drop caused by the decrease of i_{sq} is suppressed from 0.37 (p.u. value) to 0.19. The time required for voltage recovery is shortened from 86 to 46 ms. Therefore, the proposed method can optimize the voltage saturation, the voltage drop (after accelerate completion), and the current following ability during the acceleration process.

Fig. 8 shows the comparison of the system responses with and without the proposed method when suddenly applying 30% rated load. The operation speed is 120 Hz (1440 r/min). From Fig. 8(a), due to the sudden load, there is significant fluctuations in $i_{sd,q\text{-}fdb}$ and u_{fdb}, particularly between 0.1 and 0.2 s. $i_{sd,q\text{-}fdb}$ cannot correctly follow $i_{sd,q\text{-}ref}$. The maximum ripples of $i_{sd\text{-}fdb}$ and $i_{sq\text{-}fdb}$ are 3.1 and 4.8 A during the dynamic process, respectively, while the maximum voltage ripple is 0.81 (p.u. value). By contrast in the proposed decoupling method in Fig. 8(b), the dynamic performance of $i_{sd,q}$ are optimized. The maximum fluctuations of $i_{sd\text{-}fdb}$, $i_{sq\text{-}fdb}$, and u_{fdb} are suppressed to 2A, 2.4A, and 0.35, respectively.

According to Figs. 7 and 8, the mean absolute errors of i_{sd}, i_{sq}, and u_{fdb} are calculated during the transient processes, which reflects the performances of current following and voltage control in dynamic process. Table III shows the calculation results.

According to the results shown in Table III, the mean absolute error during step acceleration from 90 Hz (1080 r/min) to 140 Hz (1680 r/min) with and without the proposed method is calculated. The proposed method can reduce the mean absolute error of i_{sd} from 1.6 to 1.15 A, indicating that the following performance of i_{sd} in the transient process is improved by 28%. The mean absolute error of i_{sq} is reduced from 2.27 to 1.51 A, indicating that the following performance of i_{sq} in the transient process is improved by 33%. The mean absolute error of the

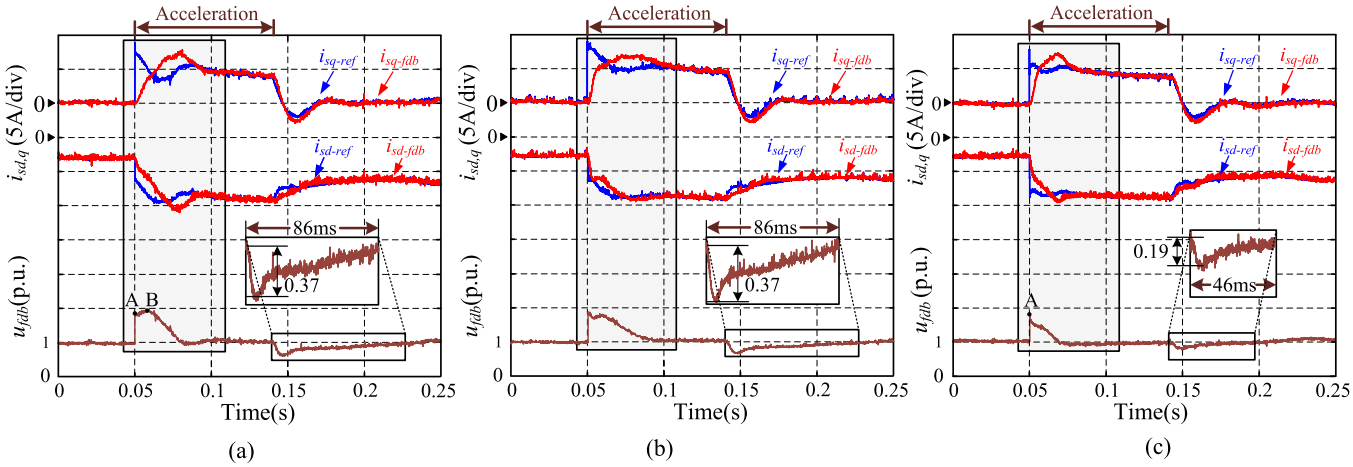

Fig. 7. Step acceleration process from 90 to 140 Hz. From top to bottom: reference and feedback values of flux current ($i_{sd\text{-}ref}$ and $i_{sd\text{-}fdb}$); reference and feedback values of torque current ($i_{sq\text{-}ref}$ and $i_{sq\text{-}fdb}$); feedback value of voltage controller (u_{fdb}). (a) Conventional method. (b) The optimized method in [6]. (c) The proposed method.

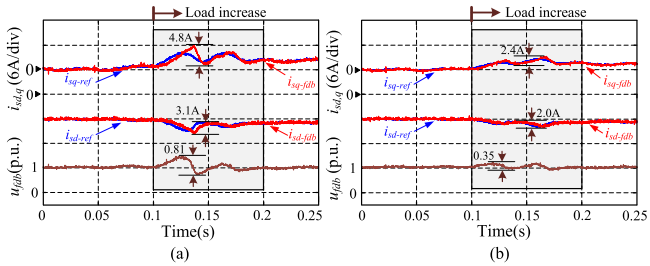

Fig. 8. System responses when suddenly applying 30% rated load. From top to bottom: $i_{sd\text{-}ref}$ and $i_{sd\text{-}fdb}$; $i_{sq\text{-}ref}$ and $i_{sq\text{-}fdb}$; u_{fdb}. (a) without the proposed method; (b) with the proposed method.

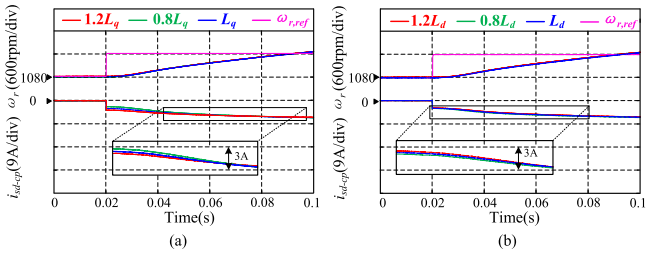

Fig. 9. Robustness test of the proposed method. (a) Impact of L_q changes. (b) Impact of L_d changes.

feedback voltage is reduced from 0.43 to 0.21, indicating that the voltage fluctuation is reduced by 51%.

Further, the current following and voltage fluctuation in the dynamic process of sudden application of 30% rated load are quantitatively analyzed. The operation speed is 120 Hz (1440 r/min). The mean absolute errors of i_{sd} and i_{sq} are 0.52 and 0.53 A with the conventional method, respectively. By contrast in the proposed method, the mean absolute errors of i_{sd} and i_{sq} are suppressed to 0.29 and 0.32 A, respectively. The current following ability of i_{sd} and i_{sq} are improved by 44% and 40% by the proposed method, respectively. The mean absolute error of the feedback voltage is reduced from 0.13 to 0.06, so the voltage fluctuation is reduced by 53%.

Fig. 9 shows the calculated compensation value (i.e., the $i_{sd\text{-}A}$ in Fig. 4) to d-axis current during the step acceleration from 90 Hz (1080 r/min) to 140 Hz (1680 r/min). The variations of L_d and L_q are set to 20% of the rated value. The calculated compensation values of the proposed method when L_q equals to 80%, 100%, and 120% of its rated value is given in Fig. 9(a), while L_d is not changed. It can be seen that variations of $i_{sd\text{-}A}$ caused by changes of L_q is small. Besides, the variation of $i_{sd\text{-}A}$ caused by changes of L_q decreases with the increasing speed, meaning that the robustness of the proposed method is improved in high-speed condition. Moreover, the calculated compensation values of the proposed method when L_d equals to 80%, 100%, and 120% of its rated value is given in Fig. 9(b), while L_q is not changed. It can be seen that variations of $i_{sd\text{-}A}$ caused by changes of L_d is also small. Moreover, compare Fig. 9(b) with Fig. 9(a), L_d changes have less effect on $i_{sd\text{-}A}$ than L_q changes, which is consistent with the analysis to the error of ICM in Section III-A.

V. Conclusion

This article reveals that the satisfactory of voltage constraint in FW region relies on the rapid coupling control between dq-axis current, especially in the transition process between maximum torque output and nonmaximum torque output. It is proved that the FW control loop can be equivalent to a cascaded structure containing three PI-type controllers in dynamic state. The excessively long chains of FW control are the root cause of failure of current coupling control as well as the voltage ripple. The quantitative analysis proved that the ICM between dq-axis current is more precise for i_{sd} compensation in dynamic process than the DCM. Comparison experiments verify the analysis-correctness and show that both the current dynamic performance and voltage saturation are optimized by applying the i_{sd} coupling compensation from ICM.

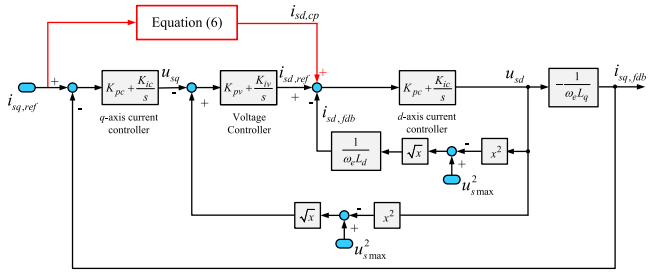

Fig. 10. Control structure diagram of the FW control loop.

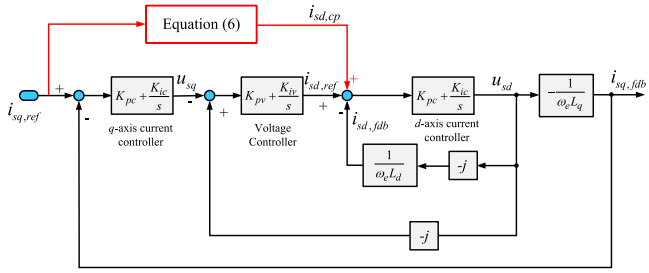

Fig. 11. Simplify of the structure in Fig. 10.

APPENDIX

This article focuses on the dynamic performance improvement of FW control. The FW control loop is expected to respond more quickly to the voltage fluctuations caused by torque changes. To achieve this target, the ICM is applied to modify the reference value of d-axis current ($i_{sd,\mathrm{ref}}$) according to the reference value of q-axis current ($i_{sq,\mathrm{ref}}$). The FW control loop contains the q-axis current controller, voltage controller, and the d-axis current controller. Fig. 10 shows the control structure diagram of the FW control loop.

In Fig. 10, the simplified motor model in (3) is used to simplify the structure diagram of the FW control loop. And the u_{smax} is treated as a disturbing term, which can be ignored for ease of analysis. On this basis, Fig. 11 shows the simplified structure diagram of the FW control loop. According to Fig. 11, the closed loop transfer functions of the FW control loop with and without the compensation $i_{sd,cp}$ of the proposed method can be expressed as (12) and (13), respectively.

Closed-loop transfer function of conventional method

$$G_C(s)=\frac{\left(K_{pc}+\frac{K_{ic}}{s}\right)\left(K_{pv}+\frac{K_{iv}}{s}\right)\left(K_{pc}+\frac{K_{ic}}{s}\right)}{\left[\left(K_{pc}+\frac{K_{ic}}{s}\right)G_v(s)-\omega_e L_q\right]\cdot G(s)}. \tag{12}$$

Closed-loop transfer function of proposed method

$$G_P(s)=\frac{\left[\left(K_{pc}+\frac{K_{ic}}{s}\right)\left(K_{pv}+\frac{K_{iv}}{s}\right)+j\frac{L_q}{L_d}\right]\cdot\left(K_{pc}+\frac{K_{ic}}{s}\right)}{\left[\left(K_{pc}+\frac{K_{ic}}{s}\right)G_v(s)-\omega_e L_q\right]\cdot G(s)}. \tag{13}$$

The $G(s)$ in (12) and (13) is

$$1+j\left(K_{p\nu}+\frac{K_{i\nu}}{s}\right)\left(K_{pc}+\frac{K_{ic}}{s}\right)+\frac{-j}{\omega_e L_d}\left(K_{pc}+\frac{K_{ic}}{s}\right). \tag{14}$$

According to (12) and (13), the characteristic equation (the denominator of the closed-loop transfer function) of the proposed method is the same as that of the conventional method. Thus, the modification to the FW loop in the proposed method does not affect the system stability.

REFERENCES

[1] N. Bedetti, S. Calligaro, and R. Petrella, "Analytical design and autotuning of adaptive flux-weakening voltage regulation loop in ipmsm drives with accurate torque regulation," *IEEE Trans. Ind. Appl.*, vol. 56, Jan./Feb., no. 1, pp. 301–313, 2020.

[2] J. Lemmens, P. Vanassche, and J. Driesen, "PMSM drive current and voltage limiting as a constraint optimal control problem," *IEEE J. Emerg. Sel. Topics Power Electron.*, vol. 3, no. 2, pp. 326–338, Jun. 2015.

[3] C. Wang, Z. Q. Zhu, and H. Zhan, "Adaptive voltage feedback controllers on nonsalient permanent magnet synchronous machine," *IEEE Trans. Ind. Appl.*, vol. 56, no. 2, pp. 1529–1542, Mar./Apr. 2020.

[4] B. Wang, J. Zhang, Y. Yu, X. Zhang, and D. Xu, "Unified complex vector field-weakening control for induction motor high-speed drives," *IEEE Trans. Power Electron.*, vol. 36, no. 6, pp. 7000–7011, Jun. 2021.

[5] Z. Dong, Y. Yu, W. Li, B. Wang, and D. Xu, "Flux-weakening control for induction motor in voltage extension region: Torque analysis and dynamic performance improvement," *IEEE Trans. Ind. Electron.*, vol. 65, no. 5, pp. 3740–3751, May 2018.

[6] Y.-C. Kwon, S. Kim, and S.-K. Sul, "Six-step operation of PMSM with instantaneous current control," *IEEE Trans. Ind. Appl.*, vol. 50, no. 4, pp. 2614–2625, Jul./Aug. 2014.

[7] X. Zhang, B. Wang, Y. Yu, J. Zhang, J. Dong, and D. Xu, "Circular arc voltage trajectory method for smooth transition in induction motor field-weakening control," *IEEE Trans. Ind. Electron.*, vol. 68, no. 5, pp. 3693–3706, May 2021.

[8] H. Wang, C. Gan, K. Ni, Z. Yu, and R. Qu, "Virtual current constraint based segmented trajectory control strategy for flux-weakening operation of SPMSM drives," *IEEE Trans. Power Electron.*, vol. 38, no. 2, pp. 2262–2274, Feb. 2023.

[9] D. Zhang, M. Zhou, C. Wang, and X. You, "Analysis and applicability comparison of single current regulator methods of PMSM under square-wave mode," *IEEE Trans. Ind. Electron.*, vol. 71, no. 2, pp. 1410–1420, Feb. 2024.

[10] Y.-C. Kwon, S. Kim, and S.-K. Sul, "Voltage feedback current control scheme for improved transient performance of permanent magnet synchronous machine drives," *IEEE Trans. Ind. Electron.*, vol. 59, no. 9, pp. 3373–3382, Sep. 2012.